Atmos. Chem. Phys. Discuss., 15, 34325–34360, 2015
www.atmos-chem-phys-discuss.net/15/34325/2015/
doi:10.5194/acpd-15-34325-2015

Atmospheric Chemistry and Physics Discussions

Tuning of a convective gravity wave source scheme based on HIRDLS observations

Q. T. Trinh[1], S. Kalisch[1], P. Preusse[1], M. Ern[1], H.-Y. Chun[2], S. D. Eckermann[3], M.-J. Kang[2], and M. Riese[1]

[1]Institute of Energy and Climate Research, Stratosphere (IEK-7), Forschungszentrum Jülich, Jülich, Germany
[2]Laboratory for Atmospheric Dynamics, Department of Atmospheric Sciences, Yonsei University, Seoul, South Korea
[3]Space Science Division, Naval Research Laboratory, Washington DC, USA

Received: 26 October 2015 – Accepted: 20 November 2015 – Published: 8 December 2015

Correspondence to: Q. T. Trinh (t.trinh@fz-juelich.de)

Published by Copernicus Publications on behalf of the European Geosciences Union.

Abstract

Convection as one dominant source of atmospheric gravity waves (GWs) has been in focus of investigation over recent years. However, its spatial and temporal forcing scales are not well known. In this work we address this open issue by a systematic verification of free parameters of the Yonsei convective GW source scheme based on observations from the High Resolution Dynamics Limb Sounder (HIRDLS). Observational constraints are taken into account by applying a comprehensive observational filter on the simulated GWs. By this approach, only long horizontal scale convective GWs are addressed. Results show that effects of long horizontal scale convective GWs can be successfully simulated by the superposition of three or four combinations of parameter sets reproducing the observed GW spectrum. These selected parameter sets are different for northern and southern summer. Although long horizontal scale waves are only part of the full spectrum of convective GWs, the momentum flux of these waves are found to be significant and relevant for the driving of the QBO. The zonal momentum balance is considered in vertical cross sections of GW momentum flux (GWMF) and GW drag (GWD). Global maps of the horizontal distribution of GWMF are considered and consistency between simulated results and HIRDLS observations is found. The latitude dependence of the zonal phase speed spectrum of GWMF and its change with altitude is discussed.

1 Introduction

Gravity waves (GWs) significantly impact global circulations by accelerating or decelerating the background wind while dissipating or breaking (e.g., McLandress, 1998; McIntyre, 1998; Kim et al., 2003; Alexander et al., 2010). For example, GWs are important in driving the quasi-biennial oscillation (QBO) (e.g., Dunkerton, 1997; Ern and Preusse, 2009; Alexander and Ortland, 2010; Evan et al., 2012; Ern et al., 2014; Kim and Chun, 2015) and the semiannual oscillation (SAO) (Ern et al., 2015). Moreover,

ACPD
15, 34325–34360, 2015

they are assumed to be the main driver of the summer-time branch of the stratospheric Brewer-Dobson circulation (Alexander and Rosenlof, 2003; Fritts and Alexander, 2003) and play a significant role in wind reversals in the mesosphere and lower thermosphere (Lindzen, 1981; Matsuno, 1982; Ern et al., 2013).

GWs are generated by different sources such as orography, convection or spontaneous adjustment of jet streams. In our work, we will focus on convectively generated GWs. Convection excites GWs via diabatic forcing by latent heat release and has long been accepted as one of the most prominent sources, in particular at low latitudes. However, convection itself is parameterized in large-domain models and global models. Even if part of the GW spectrum is resolved, physics assumptions and mathematical formulation of the convective parameterization influence the characteristics of the excited GWs (Kim et al., 2007; Preusse et al., 2014).

In order to represent in global models the important contribution of convectively forced GWs to large-scale circulations, several parameterizations of GWD induced by cumulus convection have been developed (e.g., Rind et al., 1988; Kershaw, 1995; Chun and Baik, 1998, 2002; Beres et al., 2004; Song and Chun, 2005). In this paper we focus on the convective GW source (CGWS) scheme of Song and Chun (2005). In this CGWS scheme, the spatial scale δx and the temporal scale δt of the diabatic forcing are free tunable parameters. These scales δx and δt cannot be determined from theory. Generally, there are two approaches to define these parameters: (1) forward estimation assuming typical scales of clouds or convective systems or (2) by comparing the resulting GW distributions with observations. The primary scale set MF1 of the Yonsei CGWS scheme (Song and Chun, 2005) has $\delta x = 5$ km and $\delta t = 20$ min. These scales are selected based on mesoscale simulations conducted by Song et al. (2003). The primary scale set MF1 shows good agreement with GW temperature variance (GWTV) from Microwave Limb Sounder (MLS) observations on board the Upper Atmosphere Research Satellite (Choi et al., 2009) and with GW momentum flux from three-dimensional mesoscale simulations (Choi and Chun, 2011). However, MF1 underestimates the GWTV observed by Atmospheric Infrared Sounder (AIRS) on board

ACPD
15, 34325–34360, 2015

the Aqua satellite, and therefore an additional scale set MF2 (δx = 25 km, δt = 60 min) was added (Choi et al., 2012). GWTV given by the combination of MF1 and MF2 matches AIRS observations well in both horizontal distribution and magnitude. Nevertheless, this combination cannot explain the GW spectrum observed by HIRDLS, which peaks at longer horizontal wavelength of about 600 km and vertical wavelength of about 10 km (Ern and Preusse, 2012). A possible reason is that MF1 and MF2 do not describe the presence of large-scale convective systems.

Recently, an increasing number of studies show evidence of the essential contribution of such large-scale convective systems to the global climatology. For example, in the paper of Liu and Zipser (2015), snapshots of precipitation systems (precipitation features, PFs) observed by the precipitation radar on board the Global Precipitation Mission (GPM) were analyzed. The largest PFs are found with sizes greater than 100 000 km^2. Liu and Zipser (2015) reported that PFs with size greater than 48 756 km^2 contribute 28 % of total global precipitation. For PFs with size larger than 10 000 km^2, this contribution is 54 %.

In the work of Khouider and Moncrieff (2015) a modified version of a previously developed multicloud model is used for parameterizing mesoscale convective systems (MCSs). For the condition of a typical double African and equatorial jet shear flow, a linear analysis of this modification shows an additional new scale-selective instability with a maximum of approximately 400 km. In addition, in the work of Kilpatrick and Xie (2015), surface wind observations from the Advanced SCATterometer (ASCAT) are utilized to estimate the downdrafts of MCSs. These observations show the existence of MCSs with the scale of 100–300 km.

On one hand, the GW spectra for MF1 and MF2 are not in agreement with the spectra observed by HIRDLS. On the other hand, there is an increasing number of recent studies showing the importance of large scale convective systems. This indicates a need of finding a new larger scale set for the CGWS scheme, which can correctly reproduce the spectrum observed by limb sounders. For this reason, we determine the free tunable parameters of the CGWS scheme, which provide the best agreement with HIRDLS

ACPD
15, 34325–34360, 2015

observations in this work. For that purpose a wide range of spatial and temporal scale sets of the CGWS scheme is surveyed. Based on that survey and observations from HIRDLS, combinations of scale sets which fit best to the observed GW spectrum are selected for January and July 2006. Although simulations focus on the year 2006, the current study aims to determine general characteristics of convective GWs by tuning the parameterization grounded on observations. For a further tuning of the simulated GW spectrum, the amplitude of individual waves is adjusted while keeping the same amount of total GWMF. For this purpose we compare zonal cross sections of observed and simulated GWMF and its vertical gradient. Again, the observational filter is applied to the simulations, and we can investigate the relation between absolute GWMF and GWD. Finally, we consider different source regions in global maps and discuss the interaction of GWs with the background wind employing phase speed spectra of the zonal momentum flux.

The paper is organized as follows: in Sect. 2 we introduce the model setup. The systematic survey of different scale sets for the CGWS scheme is shown in Sect. 3. Also in Sect. 3 zonal mean cross sections of GWMF, its vertical gradient, GW drag as well as global maps and GWMF spectrum in terms of zonal phase speed and latitude are presented. Finally, summary and discussion are given in Sect. 4.

2 Model setup

Simulations are performed for January and July 2006 using three main elements: first, convective GWs are generated using the CGWS scheme developed at Yonsei University (Song and Chun, 2005). The waves are propagated upward using the Gravity wave Regional Or Global RAy Tracer (GROGRAT) (Marks and Eckermann, 1995; Eckermann and Marks, 1997). Finally, a comprehensive observational filter for limb sounders (Trinh et al., 2015) is applied for comparison with HIRDLS observations. These key components of our simulation are each briefly described in a subsection below.

ACPD
15, 34325–34360, 2015

2.1 Convective gravity wave source scheme

The Yonsei CGWS scheme is described in detail by Song and Chun (2005) and here only a short summary is given. This analytical model assumes a diabatic forcing region in a three-layer atmosphere. This three-layer atmosphere has a linear wind shear increasing from U_0 at the surface to U_t at an altitude lying between bottom height and top height of the diabatic forcing. Starting from that altitude level, the background wind is constant and equals U_t. Stability of this three-layer atmosphere is characterized by a piecewise function equaling N_1 below the cloud top and N_2 above the cloud top. Momentum flux due to gravity waves is calculated from the cloud top and can be presented as a function of horizontal phase speed:

$$\overline{M}(c) = -\mathrm{sgn}(U_t - c)\rho_0 \frac{2(2\pi)^2}{L_x L_t}\left(\frac{g}{c_p T_0 N_1^2}\right)^2 \frac{N_2}{|U_t - c|}|X|^2 \Theta(c) \quad (1)$$

Here c is the horizontal ground-based phase speed, ρ_0 is the air density, L_x and L_t are appropriate spatial and temporal scales, respectively, used for averaging, c_p is the specific heat of air at constant pressure, T_0 is the reference temperature, $|X|^2$ represents resonance between vertical harmonics of natural wave modes and diabatic forcing. $|X|^2$ also represents gravity wave filtering by the vertical propagation condition. Therefore, $|X|^2$ is referred to as a wave-filtering and resonance factor. In the updated version of the CGWS scheme, Choi and Chun (2011) later redefined $\frac{N_2}{|U_t - c|}|X|^2$ as the wave-filtering and resonance factor. $\Theta(c)$ is the diabatic source function, which is assumed to have a Gaussian-shaped in space and time:

$$\Theta(c) = \frac{2q_0^2}{\delta_x}\left(\frac{\delta_x \delta_t}{16\pi}\right)^2 \frac{\sqrt{\pi/2}}{\sqrt{1 + (c - c_q)^2/c_0^2}} \quad (2)$$

ACPD
15, 34325–34360, 2015

where q_0 is the maximum magnitude of the diabatic forcing, c_q presents the moving speed of the forcing, and $c_0 = \delta_x/\delta_t$, where δ_x and δ_t are spatial and temporal scales of the forcing, respectively. δ_x and δ_t are free tunable parameters of this CGW source scheme. In this work we perform a systematic survey by running our simulations with different spatial and temporal scales. All the scales used for this survey are shown in the first two columns in Table 1.

For computational efficiency the momentum flux spectrum $\overline{M}(c)$ is not sampled continuously, but up to 10 maxima in the phase speed range from −100 to 100 m s^{-1} are selected. These discrete values are used as input for the GW ray tracer, launched at the cloud top, and propagated way from the source. Shallow heating depths are not effective in exciting far-propagating GWs. Therefore, simulations are run only for heating depths equal or larger than 3.5 km. When coupling the GW ray tracer to the CGWS scheme, there is a further tuning potential to adapt the global distributions. We can reduce the launch amplitude by a factor of $1/\sqrt{\alpha}$ and simultaneously multiply the number of launched rays by a factor of α. In this way we retain the same total GWMF at launch but reduce the amplitude of the individual waves. This may be interpreted by spreading the same total GWMF over a larger area, i.e. assuming that the wave packet has a lager spatial extent. An important consequence is that by reducing the amplitude of the individual waves, saturation is reached at higher altitudes in the atmosphere.

The latent heat input data are taken from three-hourly MERRA (modern-era retrospective analysis for research and applications) assimilated data. More detailed information about MERRA data as well as convective parameterization in MERRA can be found, for example, in Rienecker et al. (2011), Kim and Alexander (2013), and Wright and Fueglistaler (2013).

2.2 The gravity wave ray tracer

In the current work, propagation of GWs from convective GW sources into the middle atmosphere is performed using GROGRAT. Details about this ray tracer are presented in (Marks and Eckermann, 1995; Eckermann and Marks, 1997). We here only give

ACPD
15, 34325–34360, 2015

a brief description. GROGRAT is based on the full gravity wave dispersion relation, which includes both non-hydrostatic gravity waves and the Coriolis force. Wave packets are propagated according to the local group velocity of the wave depending on the wave vector and intrinsic frequency. The ray-tracing equations (Lighthill, 1967) are solved using a 4th order Runge Kutta integrator. The integration comprises the calculation of refraction of the wave vector caused by gradients of the atmospheric background in both vertical and horizontal directions. Wave action is calculated along the wave trajectory accounting for dissipation, damping, and saturation processes. Amplitude damping caused by turbulence is calculated following the work of Pitteway and Hines (1963). Radiative damping due to the temperature difference between warm and cold phases of the wave is considered following Zhu (1994). The saturated amplitude of the wave is limited using saturation criteria of Fritts and Rastogi (1985). Moreover, MERRA winds and temperature are used as atmospheric background for the ray-tracing calculations.

2.3 The comprehensive observational filter for satellite limb sounders

For comparing modeled results with HIRDLS observations, a comprehensive observational filter for satellite infrared limb sounding of gravity waves was applied. Details of this observational filter are described in Trinh et al. (2015). The observational filter considers both the visibility of waves to an infrared limb sounder and a sophisticated representation of the observation geometry. The absolute GWMF simulated by applying this observational filter to the model results can be directly compared to the GWMF from observed temperature amplitudes (Ern et al., 2004):

$$F = \frac{1}{2}\rho\frac{\lambda_z}{\lambda_h}\left(\frac{g}{N}\right)^2\left(\frac{\hat{T}}{T}\right)^2 \quad (3)$$

where F denotes absolute GWMF, ρ is the background atmosphere density, λ_z and λ_h are vertical and horizontal wavelengths, respectively, g denotes the gravity accel-

ACPD
15, 34325–34360, 2015

eration, N is the buoyancy frequency, T is the background temperature and $\hat{T}$ is the temperature amplitude of the wave.

The observational filter comprises four main processes: (1) visibility filter, (2) projection of the wavelength on the tangent-point track, (3) aliasing effect, and (4) calculation of the vertical observed wavelength. The first process (visibility filter) considers impacts caused by radiative transfer and retrieval (Preusse et al., 2002). This visibility filter directly influences the temperature amplitude $\hat{T}$. From HIRDLS observations information is provided only along measurement track. The horizontal wavelength along measurement track is generally larger than the real horizontal wavelength. The second process of the observational filter determines this along-track wavelength and the associated reduction of GWMF by modifying λ_h in Eq. (3). The aliasing effect (the third process) estimates the projection of waves towards much longer wavelengths by aliasing and the corresponding reduction of GWMF. Due to the aliasing effect, λ_h in Eq. (3) may have larger value and accordingly, F may decrease. The calculation of the vertical observed wavelength (the fourth process) addresses effects of non-vertical altitude profiles. Due to this effect, not only the vertical structure of an observed wave is sampled, but also to some extent the horizontal structure. The vertical wavelength λ_z in Eq. (3) therefore should be recalculated by considering this effect. Finally, additional corrections are applied that are required for the real satellite data to remove dominant vertical oscillation of quasi-stationary planetary waves as well as to keep only those vertical wavelengths for which amplitudes can reliably be determined in the 10 km vertical window of the MEM/HA spectral analysis (Preusse et al., 2002; Ern et al., 2011).

3 Results

3.1 A systematic survey of the Yonsei CGWS scheme

The purpose of this systematic survey is to find sets of free parameters δx and δt which describe spectra in terms of horizontal and vertical wave numbers observed by

ACPD
15, 34325–34360, 2015

HIRDLS. For the systematic survey of the spatial and temporal scales we tested the whole set of combinations given by the surveyed scales in the first two columns in Table 1. These scales are selected on one hand to cover the whole potential ranges, on the other hand with the appropriate step width to optimize computational efficiency. An appropriate step width also helps to distinguish the changing of the spectrum in the base 10 logarithmic scale of the wave numbers. Figure 1 provides an overview of the results by a reduced set of filtered, simulated GW spectra. In Fig. 1, for a better visualization, only spectra corresponding to the values given in bold in Table 1 are shown. Spectra in Fig. 1 are shown for July 2006 at the altitude of 25 km and averaged over the same regions defined as deep convection (DC) regions in Ern and Preusse (2012). These spectra are generated by binning absolute GWMF from ray-tracing calculation according to horizontal and vertical wave numbers (k_h and m) using a technique similar to that of Ern and Preusse (2012). The base 10 logarithmic scale is employed here, i.e. the x axis shows $\widetilde{k}_h = \log_{10}(1/\lambda_h)$ while the y axis shows $\widetilde{m} = \log_{10}(1/\lambda_z)$. Here λ_h and λ_z denote the horizontal and vertical wavelengths, respectively. The sizes of each bin in x and y direction are $\delta\widetilde{k}_h = 0.1$ and $\delta\widetilde{m} = 0.1$.

In Fig. 1 the color shading represents the GWMF spectra simulated by the Yonsei CGWS, propagated to observation altitude by GROGRAT and filtered according to the comprehensive observational filter. The dashed contour lines indicate the spectrum observed by HIRDLS for regions of deep convection (Ern and Preusse, 2012). For the model spectra, spatial scale increases from the right column to the left column in Fig. 1. The temporal scale increases from the bottom to the top in Fig. 1. As shown by Fig. 1, the horizontal wavelength of the spectral peak increases as the spatial scale δx of the convective system increases. Due to the resonance effect formulated in the CGWS scheme, the phase speeds and hence the vertical wavelength of the spectral peak depends only weakly on the temporal scale δt of the convective system. It can also be seen in Fig. 1 that GWs forced by convective systems with very short spatial and temporal scales (e.g. Fig. 1n, o, s, t) are strongly suppressed in HIRDLS observations due to the observational effect. Some of the spectra (e.g. Fig. 1g, h, l) show a spectral

ACPD
15, 34325–34360, 2015

peak, which locates closely to the observed spectral peak. To complement the survey grid with a parameter set providing a close match with the observed spectral peak, we calculated additional spectra with $\delta x = 200$ km and $\delta t = 150$ min for January 2006 and $\delta x = 160$ km and $\delta t = 100$ min for July 2006.

As mentioned in the introduction, the large-scale convective system studies (Liu and Zipser, 2015; Khouider and Moncrieff, 2015; Kilpatrick and Xie, 2015) indicate that CGW forcing is a multi-scale problem with major contributions by a few dominant scales. For this reason we combine several spectra from the systematic survey in order to obtain a best fit to the observed spectra. Spectra are super-imposed by minimizing the following function:

$$\eta = M_{\text{obs}} - \sum_i \zeta_i M_i \Big/ \sum_i \zeta_i \tag{4}$$

where M_i is a single spectrum from the systematic survey, ζ_i is the respective intermittency factor, and M_{obs} is the observed GWMF spectrum. Combinations of M_i with respective ζ_i, which give the best fit to the observed spectrum, are chosen from minimization of η and shown in Fig. 2c for January and Fig. 2d for July 2006. For computational efficiency, we limit the maximum number of combined spectra to 4 and only largest ζ_i are selected. The selected spatial scale δx, temporal scale δt as well as corresponding intermittency factor ζ are shown in Table 1 for January and July 2006. As shown by Fig. 2c and d, the filtered simulated spectrum matches the observed spectrum very well in both shape and location of the spectral peak for both conditions of January and July 2006. Moreover, it is noteworthy that the GW spectrum is somewhat different for northern and Southern Hemisphere, and different combinations of scale sets are needed for January and July (cf. Table 1). These scales quantitatively agree well with those found in the convective system studies, which were mentioned in the introduction. These scales determined by the regions of deep convection are then adopted for the convective sources in each hemisphere, respectively. By doing so, we assume that the observed GW spectra in these regions are dominated by CGWs. However, in other regions, other GW sources will be more dominant and direct comparison

ACPD
15, 34325–34360, 2015

with the CGWS is less meaningful or even not possible. Therefore, adopting parameter choices determined by deep convection regions for the entire respective hemisphere is one of the limitations of our approach.

In addition, in order to demonstrate effects of the observational filter, we show unfiltered combined spectra of the same selected scale sets for January 2006 in Fig. 2a and for July 2006 in Fig. 2b. Comparison of Fig. 2a–d shows that the observational filter not only reduces the magnitude, but also significantly changes the shape of the spectrum. In particular, contributions of short horizontal wavelength waves as well as short vertical wavelength waves strongly decrease and are also partly shifted to longer horizontal wavelengths. More details about effects of the observational filter on GW spectrum can be found in Trinh et al. (2015).

3.2 Zonal average of convective GWMF and its vertical gradients

In this section, our calculations are based on the scale sets of δx and δt which were selected in Sect. 3.1. Zonal averages of GWMF and its vertical gradient are calculated and shown in Fig. 3 for January and in Fig. 4 for July 2006. In all panels of Figs. 3 and 4, contour lines indicate zonal average zonal wind for the respective month. In order to generate zonal averages of absolute GWMF, the values from ray-tracing calculation are first binned onto a three-dimensional grid with bin sizes of 10° in longitude, 2° in latitude and 1 km in altitude. Results are normalized by total number of rays and the zonal averages are calculated.

Figures 3a and 4a show simulated absolute GWMF without observational filter effects for January and July, respectively. Both Figs. 3a and 4a show a main maximum of GWMF in the summer subtropics spreading from the equator to about 25° S (Fig. 3a) or to about 25° N (Fig. 4a), which is consistent with the latitude band of deep convection (e.g. Jiang et al., 2004). The width and magnitude of this maximum decreases with altitude due to wave dissipation, wave breaking and wind filtering. For January, this decrease is significant and strongly related to wind filtering at the altitude of about 20 km, where GWs encounter a wind reversal.

ACPD
15, 34325–34360, 2015

Figures 3b and 4b show filtered, simulated absolute GWMF for January and July, respectively. Due to the observational filter the magnitude of GWMF is reduced by about half an order of magnitude. Moreover, for January, stronger GWMF reduction is found at altitudes below and around the tropopause.

Observed GWMF from HIRDLS for January and July are shown in Figs. 3c and 4c, respectively. For comparing filtered, simulated GWMF (Figs. 3b and 4b) with observed GWMF (Figs. 3c and 4c) it is very important to keep in mind that the model results show GWMF only from convective sources, while observations from HIRDLS contain GWMF from a variety of sources. As convection is believed to dominate the summer subtropics, we expect model and observations to match at low latitudes while at mid and high latitudes HIRDLS observations indicate an additional enhancement due to other sources. Considering these facts, the simulated maximum in Fig. 3b and the secondary maximum in Fig. 3c in the summer subtropics match well. The same agreement can be seen by comparing Figs. 4b and 4c. In particular, centers of these maxima are both located at about 15° S for austral summer (Fig. 3b and c) or at about 15° N for boreal summer (Fig. 4b and c). Also, the structure of these maxima in the tropics from about 20 to about 40 km altitude in both simulations and observations follow the contour line of the wind reversal. However, the magnitude of the simulated maximum is somewhat lower than the observed one. Moreover, the width of the simulated maximum is slightly narrower than the observed one. These differences can be interpreted by a lack of contributions from other sources than convection.

3.2.1 Different measures of the vertical gradient

Vertical cross sections of the absolute value of GWMF span several orders of magnitude and accordingly a logarithmic color scale is used, which emphasizes the major features while the precise vertical structure is difficult to discern. On the other hand, for discussing the interaction of GWs with the background flow it is important to consider

ACPD
15, 34325–34360, 2015

the exerted zonal mean drag in the zonal direction:

$$X = -\langle 1/\rho \cdot \mathrm{d}/\mathrm{d}z(F_x)\rangle \quad (5)$$

where ρ is atmospheric density, F_x is the zonal GWMF and $\langle\ \rangle$ denotes the zonal mean. Unfortunately measurements can provide only vertical gradient P:

$$P = -\langle 1/\rho \cdot \mathrm{d}/\mathrm{d}z(|\Omega(\boldsymbol{F})|)\rangle \quad (6)$$

where $\boldsymbol{F}$ is the horizontal vector of GWMF, Ω denotes the observational filter and $|\ |$ denotes absolute values in 2-D, i.e. here $\sqrt{\Omega(F_x)^2 + \Omega(F_y)^2}$, where F_y is the meridional GWMF. In fact, differences between X and P can be significant: waves dissipating, because they reached saturation amplitudes, but propagating in opposite directions cancel each other when calculating X but contribute both positively in calculating P. Moreover, waves propagating conservatively but moving out of the observational filter Ω will enhance P but they do not contribute to the real drag X. Therefore, P may exhibit different patterns from X. However, P still emphasizes the vertical gradient and in this respect it is the closest proxy for X we can gain from measurements. The model setup of this paper allows us to calculate both X and P and hence to compare P to the observations. Furthermore, we can study the various contributions of dissipation, drag and observational filter by calculating different combinations of the vertical derivative, the observational filter and the absolute value.

3.2.2 Physical interpretation

Figures 3d and 4d show the simulated zonal drag X for January and July 2006, respectively. In the tropics (15° S–15° N) drag is exerted in regions of vertical wind shear. Positive drag is found for positive shear and negative drag for negative shear as expected for the driving of the QBO. Moreover, the magnitude of the simulated zonal drag X is comparable to the "missing drag" deduced in Ern et al. (2014). In Ern et al. (2014), in order to estimate the QBO driving by GWs, the transformed Eulerian mean zonal

ACPD
15, 34325–34360, 2015

momentum equation (Andrews et al., 1987) was utilized. All terms of this equation except the drag due to GWs were calculated using ERA-Interim assimilated data (Dee et al., 2011). The drag due to GWs is then deduced based on this equation and other calculated terms and is referred to as the "missing drag". In addition, for January 2006, Fig. 3d shows a particularly noteworthy U-shaped structure around 30 km.

Figures 3e and 4e show another type of vertical gradient of GWMF, which is calculated as follows:

$$Q = -\langle 1/\rho \cdot |\Omega(\mathrm{d}/\mathrm{d}z(\boldsymbol{F}))| \rangle \quad (7)$$

The vertical gradient Q considers the dissipation caused by those waves only which are visible to the instrument. In Fig. 3e the U-shaped structure is much less pronounced in comparison with Fig. 3d, but dissipation can be seen for a wind maximum at 40–45 km altitude and 20° S, which is located above the strongest sources and associated rather to a wind maximum than to a vertical gradient of GWMF. Similar strong dissipation can be seen at the same altitude range at about 20° N in Fig. 4e.

Figures 3f and 4f show simulated P (the quantity observations should be compared to). For January, both the U-shaped structure at around 30 km and the maximum above 40 km are visible and correspond well to similar structures in the observed vertical gradient from HIRDLS (Fig. 3g). In Fig. 3d and f, the U-shaped structure is more pronounced than in Fig. 3e. A possible reason for this difference is: in the U-shaped structure we presumably see many waves of low horizontal phase speeds which are refracted to very short vertical wavelengths and therefore are not visible to the satellite instrument. As the saturation is reached only when the vertical wavelength is even shorter than the short edge of the visibility filter, these waves propagating from below first do not pass the observational filter any longer (absence in Fig. 3f at 30 km altitude and 15° N) but dissipate almost immediately above (Fig. 3d at 30–33 km and 15° N). The dissipation itself is then not visible to the satellite (low values of vertical gradient at 30–33 km and 15° N in Fig. 3e). It should be mentioned that a related shift in the altitude of observed GWD has been discussed in Ern et al. (2014).

ACPD
15, 34325–34360, 2015

As we mentioned in Sect. 2.1, there is a further tuning potential by reducing the launch amplitude by a factor of $1/\sqrt{\alpha}$ and simultaneously multiply the number of launched rays by a factor of α. In this work, α is chosen to be 5. The choice of α does not affect the total GWMF at launch but can affect GWMF at higher altitudes and shift the saturation level to higher altitudes. Therefore, depending on the choice of α structure and magnitude of GWMF, zonal drag, simulated P, and simulated Q may be altered. With a more detailed consideration of the momentum balance this tuning factor may need to be revisited.

The GW drag maximum at 40 to 45 km altitude is seen in Fig. 3e–g, but not in Fig. 3d. This is likely caused by longer vertical wavelength waves having gained saturation amplitude but not causing much net GW drag as different propagation directions contribute. In July we find closer correspondence between P and X (again with some altitude shift). The structures of P and X also agree quite well with the structures of observed vertical gradient shown in Fig. 4g. Similar to GWMF, the observed vertical gradients in Figs. 3g and 4g are dominated, in particular at higher latitudes, by signatures from sources other than convection. It should also be noted that a 10 km vertical analysis interval is used for HIRDLS data analysis, which could also lead to some differences between model results and observations.

3.3 Horizontal distribution of GWMF and phase speed spectrum

In this section we show horizontal distributions of simulated convective GWMF as well as spectra of GWMF in terms of zonal phase speed and latitude. In Figs. 5 and 6 data for January, and in Figs. 7 and 8 data for July are shown. Figures 5 and 7 give values for 25 km altitude, while Figs. 6 and 8 give values for 40 km altitude. In each of these figures, the left column contains global maps of GWMF: panel (a) the unfiltered, simulated GWMF, panel (c) the filtered, simulated GWMF and panel (e) the observed GWMF. The right column shows zonal GWMF as a function of zonal phase speed and latitude (hereafter referred to as phase speed spectra) in bins of $4\,\mathrm{m\,s^{-1}}$ and 4°. For both maps and spectra the color scales indicate the base 10 logarithm of GWMF. As

ACPD
15, 34325–34360, 2015

for phase speed spectra GWMF with negative (westward) phase velocities is negative (westward GWMF), these values were multiplied by −1 before applying the logarithm. HIRDLS does not provide a propagation direction and accordingly phase speed cannot be deduced from the measurements.

In the global maps (panels a, c, e), the rectangle indicated by the magenta dashed line shows the low latitude area, where convection is assumed to dominate. Blank areas in panels (a), (c), (e) refer to values of GWMF, which are out of the shown value range (< -5.0 ($\log_{10}$ Pa) or > -1.0 ($\log_{10}$ Pa)). In panels (b), (d), the gray thick line indicates zonal mean of zonal wind at the considered altitude level, magenta plus line shows maximal zonal mean of zonal wind in the altitude range from cloud top to the considered altitude level, and magenta dot line shows minimal zonal mean of zonal wind in the same altitude range.

For January 2006, at 25 km altitude, high values of unfiltered GMWF are found over central south America, south Africa, a strip spreading from Madagascar to Indonesia, Indonesia and north Australia, and a strip over the Pacific ocean at around 20° S latitude spreading from 180 to 120° W (Fig. 5a). After applying the observational filter, GWMF decreases about half an order of magnitude (Fig. 5c). In addition, the observational filter also changes the distribution of GWMF at some locations. For example, over Indonesia region, a band of high GWMF at about 10° N spreading from the Philippines to 180° E, is stronger filtered out in comparison with the band of high GWMF at about 0–10° S. Figure 5e shows observed GWMF from HIRDLS. Comparison of filtered GWMF (Fig. 5c) and observed GWMF (Fig. 5e) shows a quite good agreement in location of GWMF peaks in the summer subtropics. In particular, the maxima over central south America, south Africa, Indonesia and north Australia are reproduced. The magnitude of filtered GWMF is lower in comparison with observed GWMF which, as discussed above, can be explained by a lack of other sources than convection.

The phase speed spectrum for January 2006 at 25 km altitude (Fig. 5b) shows a major peak in the tropics with eastward phase speed from several $m\,s^{-1}$ to about $25\,m\,s^{-1}$, with the center of the peak at about $5\,m\,s^{-1}$. At higher phase speeds (beyond 40–

ACPD
15, 34325–34360, 2015

50 m s^{-1}), two minor peaks in both eastward and westward directions are found. The GWMF associated with these minor peaks is about 2 orders of magnitude lower in comparison with the main peak. In mid and high latitude regions, high GWMF values are mainly associated with westward phase speeds varying from several m s^{-1} to about 40 m s^{-1}. Figure 5d shows the phase speed spectrum of filtered GWMF. The observational filter in this case reduces GWMF magnitude but almost does not impact the spectrum structure.

The effect of wind filtering can also be found in the phase speed spectrum. This effect occurs when a wave encounters the critical level, i.e. where the background wind equals the phase speed of the wave. In this case, the intrinsic phase speed and thus the vertical wavelength approach zero causing saturation and the release of GWMF. In Fig. 5b and 5d, GWMF are mainly found in the areas where GW phase speed is larger than maximal zonal mean of zonal wind (magenta plus line) or lower than minimal zonal mean of zonal wind (magenta dotted line). A small amount of GWMF still can be found in between these two lines because: (a) these lines only indicate the zonal mean of the zonal wind and thus waves may be able to propagate due to local variations and (b) many waves also have a meridional component. Still the findings indicate that filtering is dominated by the variation of the zonal wind.

For January 2006 at 40 km altitude, the horizontal band of high GWMF values in the summer subtropics becomes narrower (more concentrated around latitude of $\sim 15^{\circ}$ S) and is slightly shifted poleward. The magnitude of GWMF decreases strongly with altitude, as can be seen by comparing Figs. 5a and 6a. This is also in agreement with the vertical cross section of absolute GWMF shown in Fig. 3a. A wind reversal at about 30 km altitude is likely the main reason for the reduced GWMF values close to the equator, or in other words, for narrowing the horizontal band of high GWMF values. The location of simulated and observed GWMF hot spots agrees well (cf. Fig. 6a–c). At 40 km altitude the measurements indicate that GWMF in the hot-spot regions, where the model results suggest deep convection as the dominant source, is enhanced about one order of magnitude compared to the background regions. This is a stronger en-

ACPD
15, 34325–34360, 2015

hancement than at 25 km altitude (about half an order of magnitude) and indicates that the non-convective background is relatively less important at 40 km.

Also the phase speed spectrum changes with altitude: the main peak of the spectrum at 40 km does not stretch over the equator as for 25 km but is limited only to the Southern Hemisphere. This change is according to the change of the maximal zonal wind, which is indicated by the magenta plus line. This line surrounds the main peak in the tropics. Another major difference of the phase speed spectrum at 40 km in comparison with the one at 25 km is the absence of the peak at mid and high latitudes in the Southern Hemisphere at westward phase speeds (20 to 40° S). This absence is again likely related to wind filtering as indicated by the magenta dotted lines for the difference in minimum zonal winds in Figs. 5b, d and 6b, d, respectively.

For July 2006 at 25 km altitude, unfiltered GWMF (Fig. 7a) shows high values over the Caribbean sea, central Africa and the Asian Monsoon region. Figure 7c shows filtered GWMF with the magnitude reduced significantly due to the observational filter. Comparison of filtered GWMF (Fig. 7c) and observed GWMF (Fig. 7e) shows a quite good agreement in locations of GMWF maxima. As seen before in the zonal means, however, the observed GWMF maxima are wider, i.e. extend further to the north. In addition, the model results also show GW excitation following the warm water currents of the Gulf Stream and the Kuroshio.

Similar to January 2006 at 25 km altitude, the phase speed spectra (Fig. 7b and d) show a main peak in the summer subtropics with eastward phase speeds from several $m\,s^{-1}$ to $\sim 30\,m\,s^{-1}$. Moreover, two secondary peaks in the summer subtropics at high phase speeds (larger than 40–50 $m\,s^{-1}$), which are ~ 2.5 order of magnitude smaller in comparison with the main peak, are also found. The observational filter decreases the GWMF magnitude but almost does not alter the structure of the phase speed spectrum. This can be seen by comparing the spectrum structure shown Fig. 7b and d.

Similar to the January case, the magnitude of GWMF decreases with altitude (Fig. 8). This decrease, however, is weaker than in January. In particular, there is no strong

ACPD
15, 34325–34360, 2015

reduction of GWMF in the tropics, which narrows the region of strong GWMF between 25 and 40 km, such as for January.

Concerning the phase speed spectrum at 40 km altitude (Fig. 8b and d), a major difference in comparison with the spectrum at 25 km is much lower GWMF at mid and high latitudes in the Northern Hemisphere (from 40–80° N). This can be seen by comparing Fig. 7b and d with Fig. 8b and d. This reduction is likely related to the change of minimal zonal wind at this latitude range, which can be seen by comparing minimum zonal mean of zonal wind in Figs. 7b, d and 8b, d, respectively.

4 Summary and discussion

In this study, spatial and temporal scales of the CGWS scheme (Song and Chun, 2005) are systematically tuned to find the best match between simulated and observed horizontal and vertical wave number spectra of GWMF. The trajectory calculation for convective GWs generated by the CGWS scheme is performed using GROGRAT (Marks and Eckermann, 1995; Eckermann and Marks, 1997). For comparison with HIRDLS observations, a comprehensive observational filter (Trinh et al., 2015) is applied. The observed spectra can be well reproduced in terms of spectral shape and location of the peak by super-imposing four scale sets. The spectral shape of GWMF in the summer subtropics is different for January and July. Matching of simulated and observed spectra can only be achieved by different combinations of scale sets of the convective source indicating that this is an effect of the source properties rather than of the propagation conditions or observational filter.

We considered the contribution of these waves to the momentum balance by calculating zonal mean cross sections of absolute GWMF and its vertical gradients and compared them to respective observed quantities. The zonal average of filtered simulated GWMF is consistent with observed GWMF in the summer subtropics in both structure as well as magnitude. Applying the observational filter to the model, we find that in the mid stratosphere in regions of wind shear, slow GWs are refracted to very short

ACPD
15, 34325–34360, 2015

vertical wavelength. Consequentially, these waves cannot pass our observational filter and remain invisible whilst dissipating and exerting GWD at the location closely above the altitude where they become invisible to the instrument. Close to the stratopause waves of longer vertical wavelengths from all propagation directions reach saturation amplitudes and dissipate, in some cases without exerting much net drag. Similar to the absolute GWMF, the vertical gradient of filtered GWMF agrees well with the observed vertical gradient. Values of simulated zonal drag X are of the same order as the expected GW driving of the QBO (Ern et al., 2014). This indicates that GWs from convection organized at scales of the order of 100 km are important for driving the QBO.

Horizontal distributions of absolute unfiltered and filtered GWMF are also presented in this work. These horizontal distributions show a good agreement with observed horizontal distributions in the structure as well as the magnitude. Main convection hot spots are well reproduced. We also showed the GWMF spectra in terms of zonal phase speed and latitude. These spectra show a main peak in the tropics and summer subtropics associated with eastward phase speeds between several $\mathrm{m\,s^{-1}}$ and about $30\,\mathrm{m\,s^{-1}}$. As CGWs are commonly believed to dominate the tropics and subtropics, these phase speed spectra are expected to match respective observations of the same regions.

The vertical gradient of absolute GWMF provided by measurements is not always an indication of drag. At places where GWs have grown to reach saturation amplitudes contributions from different propagation directions cancel each other. We see such a case, for instance, in the southern subtropics around the stratopause in January. In addition, waves may leave the observational filter but do not break. For instance, it was argued by Alexander (2015) that in this way the comparison of vertical gradients of observed absolute GWMF with a momentum balance of the QBO shown by Ern et al. (2014) is not meaningful. The spectra inferred in this study show that zonal wind filtering of GWMF occurs for slow phase speed waves and in a very similar way for unfiltered and filtered simulations. Accordingly, in the zonal means there is a large

ACPD
15, 34325–34360, 2015

similarity between simulated P (the quantity corresponding to observations) and the absolute values of simulated drag Q. The only effect we can find is that waves first leave the observational filter and break soon after above, which shifts the observed "drag" downward in comparison to the real drag, an effect which was already discussed by Ern et al. (2014). Regarding wave saturation effects, it has been discussed by Ern et al. (2015) that the situation becomes more complicated if wave saturation apart from critical levels occurs. In this case, additional information about the GW spectrum may be required (for example, like pre-filtering of the GW spectrum by the winds at lower altitudes) to correctly interpret vertical gradients of observed absolute GWMF.

Due to the limitations of current global observations, the synergetic use of physics-based models, observational filter and observations using both absolute values of GWMF and its vertical gradient is currently the most promising way to infer the true properties of GWs in the atmosphere. GWs from single convective cells with horizontal scales of a few kilometers cannot be constrained by limb sounder data and exist in parallel as studies using different instruments show (Choi et al., 2009, 2012). The GWs exited by such events are clearly subgrid to global models and need to be parameterized, but also larger scale CGWs from organized convection may not well be represented depending on the convection parameterization (Ricciardulli and Garcia, 2000; Kim et al., 2007; Preusse et al., 2014) and would in this case need to be parameterized, even if the scales of potentially resulting GWs could be resolved by the dynamical core of the model.

Acknowledgements. MERRA data were provided by NASA and are available at http://disc.sci.gsfc.nasa.gov/mdisc/. HIRDLS data were provided by NASA and are available at http://disc.sci.gsfc.nasa.gov/Aura/data-holdings/HIRDLS/. This work was funded in part by the Deutsche Forschungsgemeinschaft (DFG) via the project MS-GWaves/SV (PR 919/4-1).

The article processing charges for this open-access publication were covered by a Research Centre of the Helmholtz Association.

ACPD
15, 34325–34360, 2015

References

Alexander, M. J.: Global and seasonal variations in three-dimensional gravity wave momentum flux from satellite limb-sounding temperatures, Geophys. Res. Lett., 42, 6860–6867, doi:10.1002/2015GL065234, 2015. 34345

Alexander, M. J. and Ortland, D. A.: Equatorial waves in High Resolution Dynamics Limb Sounder (HIRDLS) data, J. Geophys. Res., 115, D24111, doi:10.1029/2010JD014782, 2010. 34326

Alexander, M. J. and Rosenlof, K. H.: Gravity-wave forcing in the stratosphere: Observational constraints from the upper atmosphere research satellite and implications for parameterization in global models, J. Geophys. Res., 108, 4597, doi:10.1029/2003JD003373, 2003. 34327

Alexander, M. J., Geller, M., McLandress, C., Polavarapu, S., Preusse, P., Sassi, F., Sato, K., Eckermann, S. D., Ern, M., Hertzog, A., Kawatani, Y., Pulido, M., Shaw, T., Sigmond, M., Vincent, R., and Watanabe, S.: Recent developments in gravity wave effects in climate models, and the global distribution of gravity wave momentum flux from observations and models, Q. J. Roy. Meteor. Soc., 136, 1103–1124, doi:10.1002/qj.637, 2010. 34326

Andrews, D. G., Holton, J. R., and Leovy, C. B.: Middle Atmosphere Dynamics, vol. 40 of International Geophysics Series, Academic Press, San Diego, California, USA, 1987. 34339

Beres, J. H., Alexander, M. J., and Holton, J. R.: A method of specifying the gravity wave spectrum above convection based on latent heating properties and background wind, J. Atmos. Sci., 61, 324–337, 2004. 34327

Choi, H. J. and Chun, H. Y.: Momentum flux spectrum of convective gravity waves. Part I: An update of a parameterization using mesoscale simulation, J. Atmos. Sci, 68, 739–759, doi:10.1175/2010JAS3552.1, 2011. 34327, 34330

Choi, H.-J., Chun, H.-Y., and Song, I.-S.: Gravity wave temperature variance calculated using the ray-based spectral parameterization of convective gravity waves and its comparison with Microwave Limb Sounder observations, J. Geophys. Res., 114, D08111, doi:10.1029/2008JD011330, 2009. 34327, 34346

Choi, H.-J., Chun, H.-Y., Gong, J., and Wu, D. L.: Comparison of gravity wave temperature variances from ray-based spectral parameterization of convective gravity wave drag with AIRS observations, J. Geophys. Res., 117, D05115, doi:10.1029/2011JD016900, 2012. 34328, 34346

ACPD
15, 34325–34360, 2015

Chun, H.-Y., and Baik, J.-J.: Momentum flux by thermally induced internal gravity waves and its approximation for large-scale models, J. Atmos. Sci., 55, 3299–3310, 1998. 34327

Chun, H.-Y. and Baik, J.-J.: An updated parameterization of convectively forced gravity wave drag for use in large-scale models, J. Atmos. Sci., 59, 1006–1017, 2002. 34327

Dee, D. P., Uppala, S. M., Simmons, A. J., Berrisford, P., Poli, P., Kobayashi, S., Andrae, U., Balmaseda, M. A., Balsamo, G., Bauer, P., Bechtold, P., Beljaars, A. C. M., van de Berg, L., Bidlot, J., Bormann, N., Delsol, C., Dragani, R., Fuentes, M., Geer, A. J., Haimberger, L., Healy, S. B., Hersbach, H., Holm, E. V., Isaksen, L., Kallberg, P., Koehler, M., Matricardi, M., McNally, A. P., Monge-Sanz, B. M., Morcrette, J. J., Park, B. K., Peubey, C., de Rosnay, P., Tavolato, C., Thepaut, J. N., and Vitart, F.: The ERA-Interim reanalysis: configuration and performance of the data assimilation system, Q. J. Roy. Meteor. Soc., 137, 553–597, doi:10.1002/qj.828, 2011. 34339

Dunkerton, T. J.: The role of gravity waves in the quasi-biennial oscillation, J. Geophys. Res., 102, 26053–26076, 1997. 34326

Eckermann, S. D. and Marks, C. J.: GROGRAT: a new model of the global propagation and dissipation of atmospheric gravity waves, Adv. Space Res., 20, 1253–1256, 1997. 34329, 34331, 34344

Ern, M. and Preusse, P.: Quantification of the contribution of equatorial Kelvin waves to the QBO wind reversal in the stratosphere, Geophys. Res. Lett., 36, L21801, doi:10.1029/2009GL040493, 2009. 34326

Ern, M., and Preusse, P.: Gravity wave momentum flux spectra observed from satellite in the summertime subtropics: implications for global modeling, Geophys. Res. Lett., 39, L15810, doi:10.1029/2012GL052659, 2012. 34328, 34334

Ern, M., Preusse, P., Alexander, M. J., and Warner, C. D.: Absolute values of gravity wave momentum flux derived from satellite data, J. Geophys. Res., 109, D20103, doi:10.1029/2004JD004752, 2004. 34332

Ern, M., Preusse, P., Gille, J. C., Hepplewhite, C. L., Mlynczak, M. G., Russell III, J. M., and Riese, M.: Implications for atmospheric dynamics derived from global observations of gravity wave momentum flux in stratosphere and mesosphere, J. Geophys. Res., 116, D19107, doi:10.1029/2011JD015821, 2011. 34333

Ern, M., Preusse, P., Kalisch, S., Kaufmann, M., and Riese, M.: Role of gravity waves in the forcing of quasi two-day waves in the mesosphere: an observational study, J. Geophys. Res. Atmos., 118, 3467–3485, doi:10.1029/2012JD018208, 2013. 34327

ACPD
15, 34325–34360, 2015

Ern, M., Ploeger, F., Preusse, P., Gille, J. C., Gray, L. J., Kalisch, S., Mlynczak, M. G., Russell, J. M., and Riese, M.: Interaction of gravity waves with the QBO: a satellite perspective, J. Geophys. Res.-Atmos., 119, 2329–2355, doi:10.1002/2013JD020731, 2014. 34326, 34338, 34339, 34345, 34346

Ern, M., Preusse, P., and Riese, M.: Driving of the SAO by gravity waves as observed from satellite, Ann. Geophys., 33, 483–504, doi:10.5194/angeo-33-483-2015, 2015. 34326, 34346

Evan, S., Alexander, M. J., and Dudhia, J.: WRF simulations of convectively generated gravity waves in opposite QBO phases, J. Geophys. Res., 117, D12117, doi:10.1029/2011JD017302, 2012. 34326

Fritts, D. and Alexander, M.: Gravity wave dynamics and effects in the middle atmosphere, Rev. Geophys., 41, 1003, doi:10.1029/2001RG000106, 2003. 34327

Fritts, D. C. and Rastogi, P. K.: Convective and dynamical instabilities due to gravity wave motions in the lower and middle atmosphere: theory and observations, Radio Sci., 20, 1247–1277, 1985. 34332

Jiang, J., Wang, B., Goya, K., Hocke, K., Eckermann, S., Ma, J., Wu, D., and Read, W.: Geographical distribution and interseasonal variability of tropical deep convection: UARS MLS observations and analyses, J. Geophys. Res.-Atmos., 109, D03111, doi:10.1029/2003JD003756, 2004. 34336

Kershaw, R.: Parametrization of momentum transport by convectively generated gravity waves, Q. J. Roy. Meteor. Soc., 121, 1023–1040, doi:10.1002/qj.49712152505, 1995. 34327

Khouider, B. and Moncrieff, M. W.: Organized convection parameterization for the ITCZ, J. Atmos. Sci., 72, 3073–3096, doi:10.1175/JAS-D-15-0006.1, 2015. 34328, 34335

Kilpatrick, T. J. and Xie, S.-P.: ASCAT observations of downdrafts from mesoscale convective systems, Geophys. Res. Lett., 42, 1951–1958, doi:10.1002/2015GL063025, 2015. 34328, 34335

Kim, J.-E. and Alexander, M. J.: Tropical precipitation variability and convectively coupled equatorial waves on submonthly time scales in reanalyses and TRMM, J. Climate, 26, 3013–3030, doi:10.1175/JCLI-D-12-00353.1, 2013. 34331

Kim, S.-Y., Chun, H.-Y., and Baik, J.-J.: Sensitivity of typhoon-induced gravity waves to cumulus parameterizations, Geophys. Res. Lett., 34, L15814, doi:10.1029/2007GL030592, 2007. 34327, 34346

ACPD
15, 34325–34360, 2015

Kim, Y.-H. and Chun, H.-Y.: Contributions of equatorial wave modes and parameterized gravity waves to the tropical QBO in HadGEM2, J. Geophys. Res.-Atmos., 120, 1065–1090, doi:10.1002/2014JD022174, 2015. 34326

Kim, Y.-J., Eckermann, S. D., and Chun, H.-Y.: An overview of the past, present and future of gravity-wave drag parameterization for numerical climate and weather prediction models – Survey article, Atmos. Ocean, 41, 65–98, doi:10.3137/ao.410105, 2003. 34326

Lighthill, M. J.: Waves in fluids, Commun. Pur. Appl. Math., 20, 267–293, doi:10.1002/cpa.3160200204, 1967. 34332

Lindzen, R. S.: Turbulence and stress owing to gravity wave and tidal breakdown, J. Geophys. Res., 86, 9707–9714, 1981. 34327

Liu, C. and Zipser, E. J.: The global distribution of largest, deepest, and most intense precipitation systems, Geophys. Res. Lett., 42, 3591–3595, doi:10.1002/2015GL063776, 2015. 34328, 34335

Marks, C. J. and Eckermann, S. D.: A three-dimensional nonhydrostatic ray-tracing model for gravity waves: formulation and preliminary results for the middle atmosphere, J. Atmos. Sci., 52, 1959–1984, 1995. 34329, 34331, 34344

Matsuno, T.: A quasi one-dimensional model of the middle atmosphere circulation interacting with internal gravity waves, J. Meteorol. Soc. Jpn., 60, 215–226, 1982. 34327

McIntyre, M. E.: Breaking waves and global scale chemical transport in the Earth's atmosphere, with spinoffs for the Sun's interior, Prog. Theor. Phys., 130, 137–166, 1998. 34326

McLandress, C.: On the importance of gravity waves in the middle atmosphere and their parameterization in general circulation models, J. Atmos. Terr. Phys., 60, 1357–1383, 1998. 34326

Pitteway, M. L. V. and Hines, C. O.: The viscous damping of atmospheric gravity waves, Can. J. Phys., 41, 1935–1948, doi:10.1139/p63-194, 1963. 34332

Preusse, P., Dörnbrack, A., Eckermann, S. D., Riese, M., Schaeler, B., Bacmeister, J. T., Broutman, D., and Grossmann, K. U.: Space-based measurements of stratospheric mountain waves by CRISTA, 1. Sensitivity, analysis method, and a case study, J. Geophys. Res., 107, 8178, doi:10.1029/2001JD000699, 2002. 34333

Preusse, P., Ern, M., Bechtold, P., Eckermann, S. D., Kalisch, S., Trinh, Q. T., and Riese, M.: Characteristics of gravity waves resolved by ECMWF, Atmos. Chem. Phys., 14, 10483–10508, doi:10.5194/acp-14-10483-2014, 2014. 34327, 34346

ACPD
15, 34325–34360, 2015

Ricciardulli, L. and Garcia, R. R.: The excitation of equatorial waves by deep convection in the NCAR Community Climate Model (CCM3), J. Atmos. Sci., 57, 3461–3487, 2000. 34346

Rienecker, M. M., Suarez, M. J., Gelaro, R., Todling, R., Bacmeister, J., Liu, E., Bosilovich, M. G., Schubert, S. D., Takacs, L., Kim, G.-K., Bloom, S., Chen, J., Collins, D., Conaty, A., da Silva, A., Gu, W., Joiner, J., Koster, R. D., Lucchesi, R., Molod, A., Owens, T., Pawson, S., Pegion, P., Redder, C. R., Reichle, R., Robertson, F. R., Ruddick, A. G., Sienkiewicz, M., and Woollen, J.: MERRA: NASA's modern-era retrospective analysis for research and applications, J. Climate, 24, 3624–3648, doi:10.1175/JCLI-D-11-00015.1, 2011. 34331

Rind, D., Suozzo, R., Balachandran, N. K., Lacis, A., and Russell, G.: The GISS global climate-middle atmosphere model. Part I: Model structure and climatology, J. Atmos. Sci., 45, 329–370, doi:10.1175/1520-0469(1988)045<0329:TGGCMA>2.0.CO;2, 1988. 34327

Song, I. S. and Chun, H. Y.: Momentum flux spectrum of convectively forced internal gravity waves and its application to gravity wave drag parameterization. Part I: Theory, J. Atmos. Sci., 62, 107–124, 2005. 34327, 34329, 34330, 34344

Song, I.-S., Chun, H.-Y., and Lane, T. P.: Generation mechanisms of convectively forced internal gravity waves and their propagation to the stratosphere, J. Atmos. Sci., 60, 1960–1980, 2003. 34327

Trinh, Q. T., Kalisch, S., Preusse, P., Chun, H.-Y., Eckermann, S. D., Ern, M., and Riese, M.: A comprehensive observational filter for satellite infrared limb sounding of gravity waves, Atmos. Meas. Tech., 8, 1491–1517, doi:10.5194/amt-8-1491-2015, 2015. 34329, 34332, 34336, 34344

Wright, J. S. and Fueglistaler, S.: Large differences in reanalyses of diabatic heating in the tropical upper troposphere and lower stratosphere, Atmos. Chem. Phys., 13, 9565–9576, doi:10.5194/acp-13-9565-2013, 2013. 34331

Zhu, X.: A new theory of the saturated gravity wave spectrum for the middle atmosphere, J. Atmos. Sci., 51, 3615–3626, 1994. 34332

ACPD
15, 34325–34360, 2015

Table 1. Surveyed and selected spatial and time scales (δx, δt) as well as intermittency factor (ζ) for the Yonsei CGWS scheme. Numbers in bold denote the scales, which are shown in Fig. 1.

Scales used for surveying		Selected scales for January			Selected scales for July		
δx (km)	δt (min)	δx (km)	δt (min)	ζ	δx (km)	δt (min)	ζ
4	**10**	80	240	1.0	40	80	1.0
8	20	120	120	0.4	160	100	1.0
12	**40**	200	150	0.4	250	240	1.0
25	80	250	360	0.7			
40	**120**						
80	240						
120	360						
250	**720**						
400							
800							
1200							

ACPD
15, 34325–34360, 2015

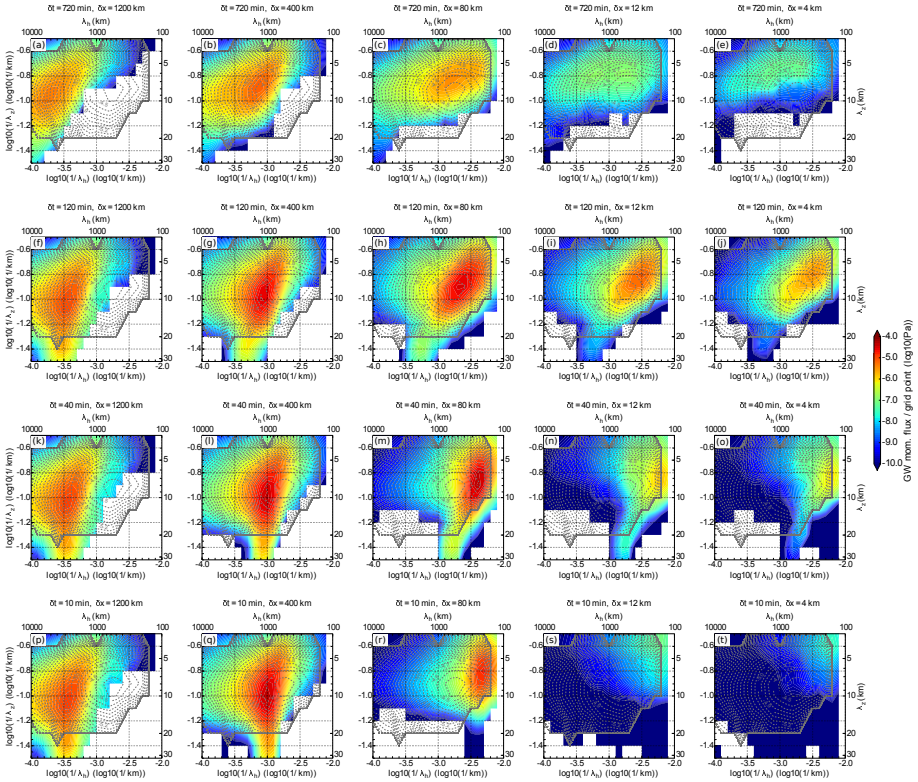

Figure 1. A systematic survey of the CGWS scheme depending on different spatial and temporal scales of the convective system for July 2006. The color code shows the simulated GWMF spectra of CGWs generated by the Yonsei CGWS scheme, propagated upward to 25 km altitude using GROGRAT and filtered according to the observational filter. The dashed contour lines show the spectrum for regions of deep convection observed by HIRDLS.

ACPD
15, 34325–34360, 2015

Tuning a convective GW source scheme based on satellite observations

Q. T. Trinh et al.

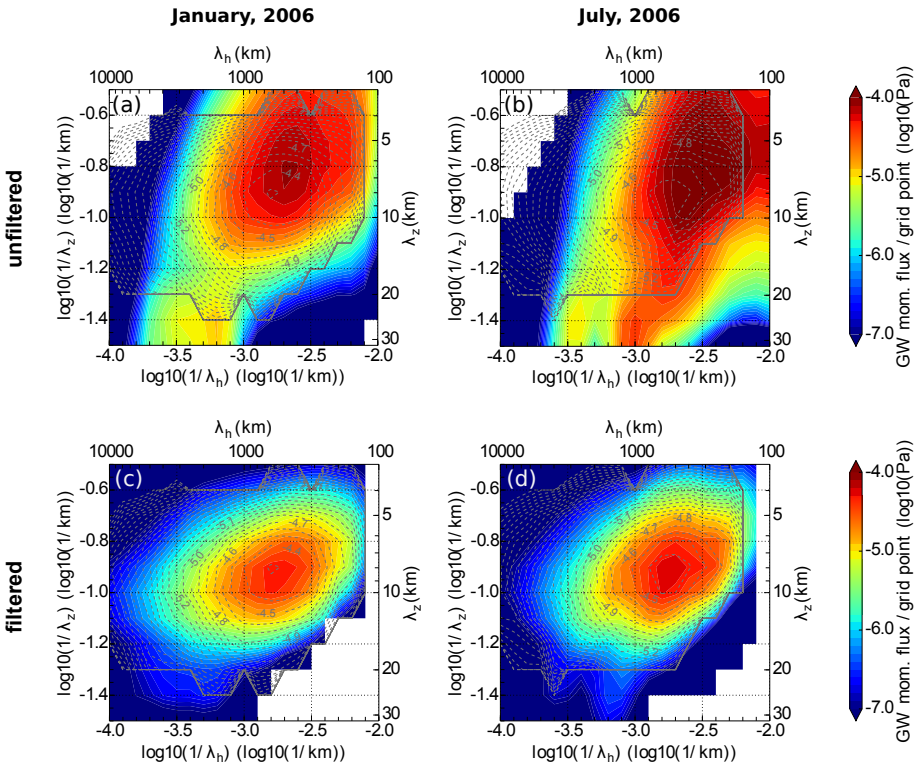

Figure 2. Unfiltered combined GW spectra of selected scale sets for **(a)** January 2006 and **(b)** July 2006 and filtered combined spectra of selected scale sets for **(c)** January 2006 and **(d)** July 2006. All spectra are shown for the altitude level of 25 km. The color code represents combined filtered simulated spectra; the dashed contour lines represent spectra observed by HIRDLS for regions of deep convection.

ACPD
15, 34325–34360, 2015

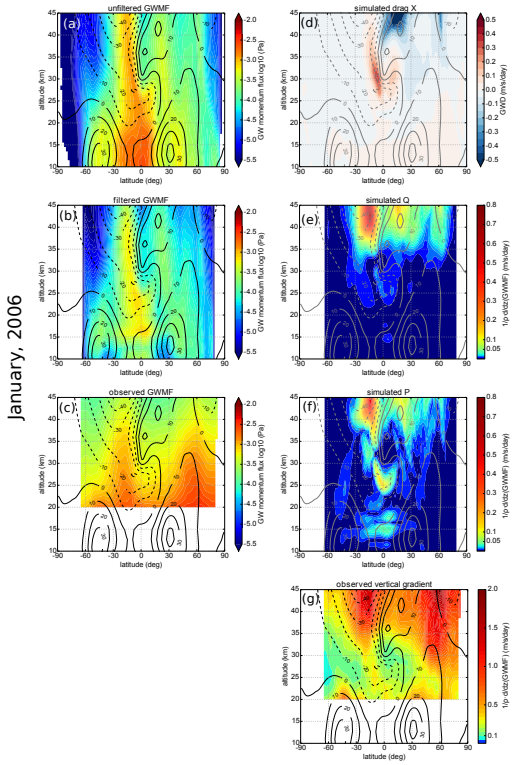

Figure 3. Comparison of simulated GWMF and its vertical gradients with observations from HIRDLS for January 2006. Panel **(a)** shows simulated unfiltered absolute GWMF. Panel **(b)** shows simulated filtered absolute GWMF. Panel **(c)** shows absolute GWMF observed by HIRDLS. Panel **(d)** shows simulated zonal GW drag. Panel **(e)** shows simulated vertical gradient Q. Panel **(f)** shows simulated vertical gradient P. Panel **(g)** shows observed vertical gradient of absolute GWMF from HIRDLS. For details see text.

ACPD
15, 34325–34360, 2015

Tuning a convective GW source scheme based on satellite observations

Q. T. Trinh et al.

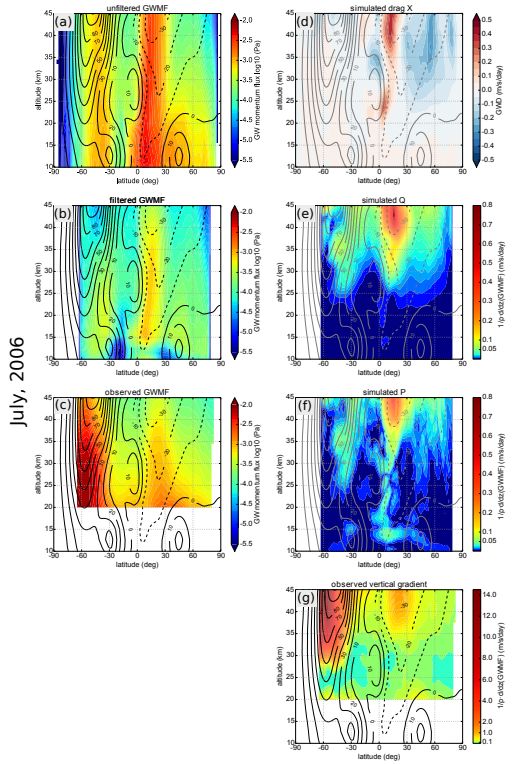

Figure 4. Comparison of simulated GWMF and its vertical gradients with observations from HIRDLS for July 2006. Panel **(a)** shows simulated unfiltered absolute GWMF. Panel **(b)** shows simulated filtered absolute GWMF. Panel **(c)** shows absolute GWMF observed by HIRDLS. Panel **(d)** shows simulated zonal GW drag. Panel **(e)** shows simulated vertical gradient Q. Panel **(f)** shows simulated vertical gradient P. Panel **(g)** shows observed vertical gradient of absolute GWMF from HIRDLS. For details see text.

ACPD
15, 34325–34360, 2015

Tuning a convective GW source scheme based on satellite observations

Q. T. Trinh et al.

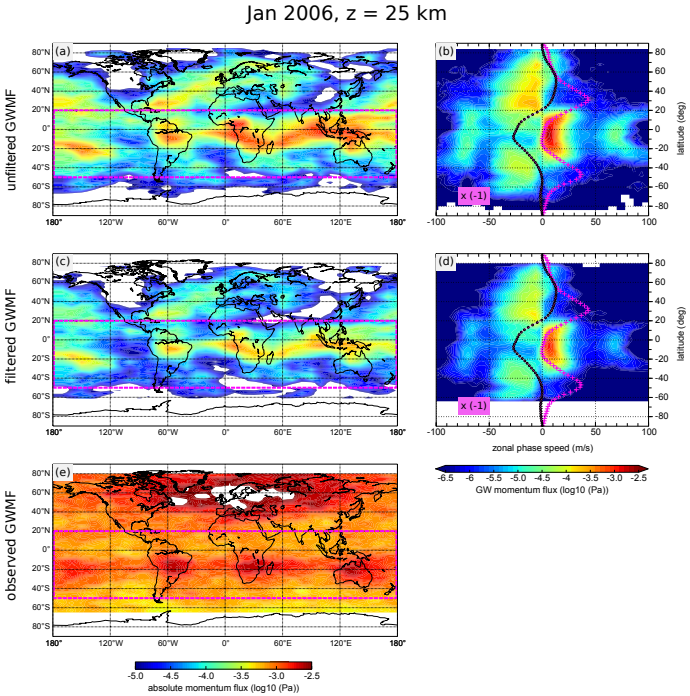

Figure 5. Horizontal distribution of **(a)** unfiltered absolute GWMF and **(c)** filtered absolute GWMF in comparison with **(e)** horizontal distribution of observed absolute GWMF. Panel **(b)** shows phase speed spectrum of unfiltered zonal GWMF (absolute values) and panel **(d)** shows phase speed spectrum of filtered zonal GWMF (absolute values). In phase speed spectra, GWMF values associated with negative values of phase speed (on the left-hand side) are multiplied with −1. Results are shown for January 2006 at 25 km altitude. For details see text.

ACPD
15, 34325–34360, 2015

Tuning a convective GW source scheme based on satellite observations

Q. T. Trinh et al.

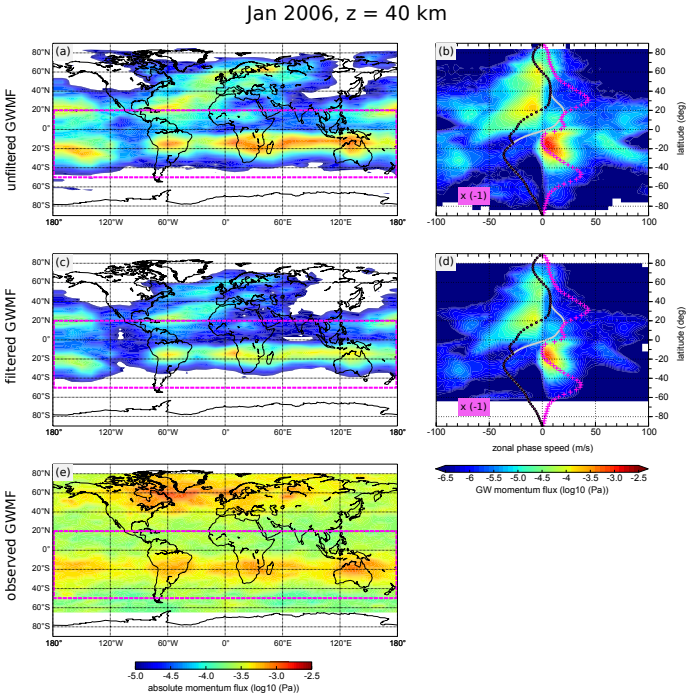

Figure 6. Horizontal distribution of **(a)** unfiltered absolute GWMF and **(c)** filtered absolute GWMF in comparison with **(e)** horizontal distribution of observed absolute GWMF. Panel **(b)** shows phase speed spectrum of unfiltered zonal GWMF (absolute values) and panel **(d)** shows phase speed spectrum of filtered zonal GWMF (absolute values). In phase speed spectra, GWMF values associated with negative values of phase speed (on the left-hand side) are multiplied with −1. Results are shown for January 2006 at 40 km altitude. For details see text.

ACPD
15, 34325–34360, 2015

Tuning a convective GW source scheme based on satellite observations

Q. T. Trinh et al.

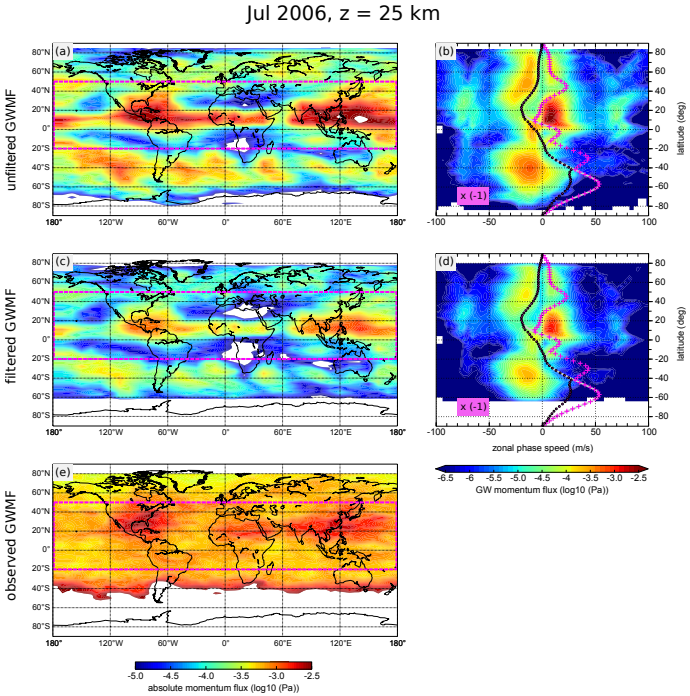

Figure 7. Horizontal distribution of **(a)** unfiltered absolute GWMF and **(c)** filtered absolute GWMF in comparison with **(e)** horizontal distribution of observed absolute GWMF. Panel **(b)** shows phase speed spectrum of unfiltered zonal GWMF (absolute values) and panel **(d)** shows phase speed spectrum of filtered zonal GWMF (absolute values). In phase speed spectra, GWMF values associated with negative values of phase speed (on the left-hand side) are multiplied with −1. Results are shown for July 2006 at 25 km altitude. For details see text.

ACPD
15, 34325–34360, 2015

Tuning a convective GW source scheme based on satellite observations

Q. T. Trinh et al.

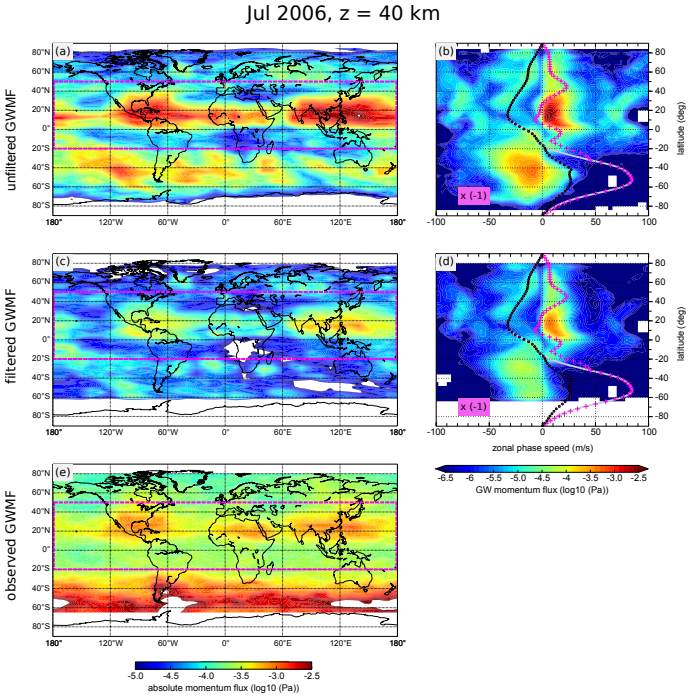

Figure 8. Horizontal distribution of **(a)** unfiltered absolute GWMF and **(c)** filtered absolute GWMF in comparison with **(e)** horizontal distribution of observed absolute GWMF. Panel **(b)** shows phase speed spectrum of unfiltered zonal GWMF (absolute values) and panel **(d)** shows phase speed spectrum of filtered zonal GWMF (absolute values). In phase speed spectra, GWMF values associated with negative values of phase speed (on the left-hand side) are multiplied with −1. Results are shown for July 2006 at 40 km altitude. For details see text.

ACPD
15, 34325–34360, 2015

Tuning a convective GW source scheme based on satellite observations

Q. T. Trinh et al.